Transmission optical coherence tomography based measurement of optical material properties

A. K. Trull,[1,2] **J. van der Horst,**[1,2] **J. G. Bijster,**[1] **and J. Kalkman**[1,*]

[1]*Department of Imaging Physics, Delft University of Technology, Lorentzweg 1, 2628 CJ Delft, The Netherlands*
[2]*These authors contributed equally to this work*
[*] *j.kalkman@tudelft.nl*

Abstract: We present transmission optical coherence tomography (transmission OCT) as a versatile tool to measure optical material properties of turbid media. The transmission OCT signal is described in detail and it is demonstrated how the group refractive index (n_g), group velocity dispersion (GVD) and optical attenuation can be determined from this signal. We experimentally validate the refractive index properties of glasses, liquids and glucose water solutions in terms of n_g and GVD. Measurements of scattering coefficients are determined using transmission OCT for suspensions of silica particles. Quantitative agreement is obtained with a dependent scattering model, both for the average as well as the wavenumber resolved optical attenuation coefficient. Good agreement is observed between our measurements and literature values.

OCIS codes: (020.1670) Coherent optical effects; (170.4500) Optical coherence tomography; (290.4210) Multiple scattering; (290.7050) Turbid media.

References and links

1. G. Zaccanti, S. Del Bianco, and F. Martelli, "Measurements of optical properties of high-density media," Appl. Opt. **42**, 4023–4030 (2003).
2. R. H. Bremmer, S. C. Kanick, N. Laan, A. Amelink, T. G. van Leeuwen, and M. C. Aalders, "Non-contact spectroscopic determination of large blood volume fractions in turbid media," Biomed. Opt. Express **2**, 396–407 (2011).
3. B. Aernouts, E. Zamora-Rojas, R. Van Beers, R. Watté, L. Wang, M. Tsuta, J. Lammertyn, and W. Saeys, "Supercontinuum laser based optical characterization of Intralipid® phantoms in the 500-2250 nm range," Opt. Express **21**, 32450–32467 (2013).
4. K. Barwari, D. M. de Bruin, E. C. Cauberg, D. J. Faber, T. G. van Leeuwen, H. Wijkstra, J. de la Rosette, and M. P. Laguna, "Advanced diagnostics in renal mass using optical coherence tomography: a preliminary report," J. Endourol. **25**, 311–315 (2011).
5. N. Bosschaart, D. J. Faber, T. G. van Leeuwen, and M. C. Aalders, "In vivo low-coherence spectroscopic measurements of local hemoglobin absorption spectra in human skin," J. Biomed. Opt. **16**, 100504–100504 (2011).
6. A. V. Zvyagin, K. K. Silva, S. A. Alexandrov, T. R. Hillman, J. J. Armstrong, T. Tsuzuki, and D. Sampson, "Refractive index tomography of turbid media by bifocal optical coherence refractometry," Opt. Express **11**, 3503–3517 (2003).
7. J. J. J. Dirckx, L. C. Kuypers, and W. F. Decraemer, "Refractive index of tissue measured with confocal microscopy," J. Biomed. Opt. **10**, 044014–044014 (2005).
8. Z. Wang, K. Tangella, A. Balla, G. Popescu, "Tissue refractive index as marker of disease," J. Biomed. Opt. **11**, 116017-1160177(2011).

#251546 Received 8 Oct 2015; revised 1 Dec 2015; accepted 1 Dec 2015; published 18 Dec 2015

9. M. R. Hee, E. A. Swanson, J. A. Izatt, J. M. Jacobson, and J. G. Fujimoto, "Femtosecond transillumination optical coherence tomography," Opt. Lett **18**, 950–952 (1993).
10. V. D. Nguyen, D. J. Faber, E. van der Pol, T. G. van Leeuwen, and J. Kalkman, "Dependent and multiple scattering in transmission and backscattering optical coherence tomography," Opt. Express **21**, 29145–29156 (2013).
11. S. Kedenburg, M. Vieweg, T. Gissibl, and H. Giessen, "Linear refractive index and absorption measurements of nonlinear optical liquids in the visible and near-infrared spectral region," Opt. Mater. Express **2**, 1588–1611 (2012).
12. Y. Verma, P. Nandi, K. D. Rao, M. Sharma, and P. K. Gupta, "Use of common path phase sensitive spectral domain optical coherence tomography for refractive index measurements," Appl. Optics **50**, E7–E12 (2011).
13. A. F. Fercher, C. K. Hitzenberger, M. Sticker, R. Zawadzki, B. Karamata, and T. Lasser, "Numerical dispersion compensation for partial coherence interferometry and optical coherence tomography," Opt. Express **9**, 610–615 (2001).
14. N. Nassif, B. Cense, B. Park, M. Pierce, S. Yun, B. Bouma, G. J. Tearney, T. C. Chen, and J. F. de Boer, "In vivo high-resolution video-rate spectral-domain optical coherence tomography of the human retina and optic nerve," Opt. Express **12**, 367–376 (2004).
15. C. Mätzler, "MATLAB functions for Mie scattering and absorption, version 2," IAP Res. Rep. **8** (2002).
16. Schott, "Optical glass data sheets," (2012).
17. Hikari, "Optical catalogue," (2015).
18. Sumita, "Optical glass," (2015).
19. I. H. Malitson, "Interspecimen comparison of the refractive index of fused silica," J. Opt. Soc. Am. **55**, 1205–1208 (1965).
20. B. Tatian, "Fitting refractive-index data with the sellmeier dispersion formula," Appl. Optics **23**, 4477–4485 (1984).
21. Heraeus, *Quartz Glass for Optics Data and Properties*(2015).
22. I. H. Malitson, "Refraction and dispersion of synthetic sapphire," J. Opt. Soc. Am. **52**, 1377–1379 (1962).
23. W. C. Tan, K. Koughia, J. Singh, and S. O. Kasap, "Fundamental optical properties of materials I," in *Optical Properties of Condensed Matter and Applications,* Jai Singh (John Wiley and Sons, Ltd, Chichester, UK. 2006)
24. H. H. Li, "Refractive index of alkaline earth halides and its wavelength and temperature derivatives," J. Phys. and Chem. Ref. Data **9**, 161–290 (1980).
25. M. Daimon and A. Masumura, "High-accuracy measurements of the refractive index and its temperature coefficient of calcium fluoride in a wide wavelength range from 138 to 2326 nm," Appl. Optics **41**, 5275–5281 (2002).
26. I. H. Malitson, "A redetermination of some optical properties of calcium fluoride," Appl. Optics **2**, 1103–1107 (1963).
27. M. Daimon and A. Masumura, "Measurement of the refractive index of distilled water from the near-infrared region to the ultraviolet region," Appl Optics **46**, 3811–3820 (2007).
28. J. Rheims, J. Köser, and T. Wriedt, "Refractive-index measurements in the near-IR using an Abbe refractometer," Meas. Sci. Technol. **8**, 601 (1997).
29. W. M. Yunus and A. B. Rahman, "Refractive index of solutions at high concentrations," Appl. Optics **27**, 3341–3343 (1988).
30. S. R. Kachiraju and D. A. Gregory, "Determining the refractive index of liquids using a modified Michelson interferometer," Opt and Laser Technol **44**, 2361–2365 (2012).

1. Introduction

Optical material properties are important in the field of optics where they are paramount to the production of high quality optical components. Also in other fields such as pharmaceuticals, medical imaging, photo-dynamic therapy and food production are optical material properties important for quality control and diagnostics. However, in contrast to optical materials such as glasses, the optical materials in these fields are turbid, i.e., they have both optical absorption and scattering. Consequently, the characterization of their optical properties such as refractive index (dispersion) and optical attenuation is a lot more challenging.

Collimated transmission measurements, for example, can be used to measure the total attenuation coefficient of turbid media [1]. However, the difficulty with this method is to avoid measuring scattered light on the detector, which is done using pinholes and long path lengths, but nevertheless restricts the measurements to relatively thin samples. Diffuse reflectance spectroscopy has been used to measure the wavelength dependent absorption coefficient and the reduced scattering coefficient to identify the age of bloodstains, where the change of hemoglobin

#251546 Received 8 Oct 2015; revised 1 Dec 2015; accepted 1 Dec 2015; published 18 Dec 2015

fractions can be observed over time [2]. Yet, diffuse reflectance spectroscopy requires the use of transport theory to calculate the optical properties. Consequently, this technique is limited to samples that are homogeneous or have a known structure. A combination of transmittance and diffuse reflectance measurements can also be used to determine the absorption coefficient, the scattering coefficient and the scattering anisotropy of turbid media [3], but also suffers from the above mentioned effects.

Some techniques are capable of measuring the spatial variation in optical properties, producing an image of the sample. Optical coherence tomography (OCT) has been used to measure light attenuation of tissue and is able to differentiate between normal and tumorous tissue [4]. Low-coherence spectroscopy has been used to image the wavelength dependent absorption and scattering coefficient in vivo in the human skin [5]. Imaging of the refractive index in turbid media has been shown using bifocal OCT [6]. By measuring the optical path length between two focal spots in a sample the refractive index can be obtained. It is also possible to measure the refractive index of turbid media using confocal microscopy [7]. In this case, a layer of immersion fluid of the same thickness as the sample is used in combination with a calibrated z-stage movement. Optical properties of tissue can provide functional information regarding its biological state. The use of optical techniques for biopsies has been shown for example by Wang et al. [8], who demonstrated quantitative phase imaging of breast and prostate biopsies to identify tumour calcifications.

All the techniques described above only provide measurement of either the refractive index or the attenuation coefficients. Part of these techniques rely only on diffuse light while others suffer from it, causing restrictions on the sample size and the type of sample.

Here, we present Fourier-domain transmission optical coherence tomography (transmission OCT) that is used to determine both the refractive index and optical attenuation coefficients. Transmission OCT was first used by Hee et al. [9] for imaging of objects embedded in turbid media. Recently, transmission OCT has been used to measure the scattering coefficient μ_s in turbid media [10]. We show that transmission OCT can provide an estimation of the group refractive index, n_g, the group velocity dispersion, GVD, as well as the (spectrally resolved) total attenuation coefficient of the material. The advantage of using transmission OCT is the combination of confocal gating and path-length selectivity (coherence gating). This allows for a strong rejection of scattered light, as well as the possibility to further filter out multiple scattered light.

First, a theoretical framework is provided that describes the transmission OCT in the presence of attenuation and dispersion. Second, the experimental setup is described together with an algorithm to analyze the experimental data. Finally, experimental data is presented that demonstrates the proposed techniques.

2. Theory

2.1. The transmission Fourier domain OCT signal

Transmission OCT is based on the interaction of light in the sample arm of a Mach-Zehnder interferometer with light propagating in the reference arm. A schematic diagram of the Mach-Zehnder interferometer with spectral-domain detection as used for transmission OCT is given in Fig. 1. The experimental realization of the setup is described in more detail in Section 3.1.

Light from the light source is launched into the interferometer. The source intensity spectrum is given by $S(k) = E_s(k)^* E_s(k)$, with $*$ denoting complex conjugation, k is wavenumber in vacuum $k = 2\pi/\lambda$ and $E_s(k)$ are plane electromagnetic waves. In the following, we assume one-dimensional rectilinear propagation of scalar plane waves light field through the interferometer. Polarization and multiple scattering are neglected in our model. Due to averaging over many optical cycles, the time dependence of the signals is disregarded and all parameters are real

#251546 Received 8 Oct 2015; revised 1 Dec 2015; accepted 1 Dec 2015; published 18 Dec 2015

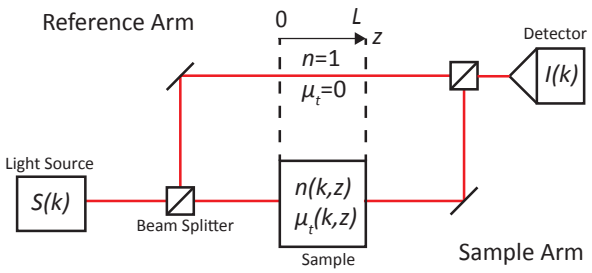

Fig. 1. Schematic diagram of the Fourier-domain transmission OCT system. $I(k)$: detected intensity at the spectrometer, L: length of the sample, $n(k,z)$: refractive index of the sample, $\mu_t(k,z)$: total attenuation, $S(k)$: source intensity.

numbers unless stated otherwise. We neglect any path lengths and phase factor that are equal for both interferometer arms. The incoming beam is first split and later combined by an ideal beam splitter with an (intensity) reflection coefficient of α and transmission coefficient $1-\alpha$.

For the light wave propagating in the reference arm we assume it to be filled with air, i.e. the refractive index is unity, $n(k,z)=1$ and there is no attenuation, $\mu(k,z)=0$. Assuming ideal mirrors in the interferometer with unity reflectivity, the reference arm field $E_{ref}(k)$ at the detector is given by

$$E_{ref}(k) = [\alpha(1-\alpha)]^{\frac{1}{2}} E_s(k) \exp(ikL), \tag{1}$$

where $i=(-1)^{1/2}$, and where L is the physical length equal to the physical length in the sample arm in which interaction takes place. After interaction with a sample of length L in the sample arm the field from the sample arm falling on the detector is

$$E_{sam}(k) = [\alpha(1-\alpha)]^{\frac{1}{2}} E_s(k) \exp\left(-\frac{1}{2}\int_0^L \mu_t(k,z)dz\right) \exp\left(ik\int_0^L n(k,z)dz\right), \tag{2}$$

where $\mu_t(k,z)$ is the total attenuation coefficient and L is the distance along the optical path in the sample arm where interaction takes place. In the following we consider only homogeneous media, i.e. $\mu(k,z)=\mu(k)$ and $n(z,k)=n(k)$, and the integrals are replaced by multiplications with L. The total intensity at the detector $I(k)=(E_{ref}(k)+E_{sam}(k))(E_{ref}(k)+E_{sam}(k))^*$ consists of the reference arm intensity, the sample arm intensity and the cross terms which contain the interference signal. Combining Eq. (1) and Eq. (2), and retaining only the interference term of the intensity on the detector we obtain

$$I_{int}(k) = 2\alpha(1-\alpha)E_s^2(k) \exp\left(-\frac{1}{2}L\mu_t(k)\right) \cos[kL(n(k)-1)]. \tag{3}$$

The measured interference signal is proportional to an exponential factor describing the optical attenuation and is proportional to a cosine with a phase that is modulated by the spectral variation of the refractive index (dispersion).

2.2. *Material dispersion*

The term $n(k)-1$ in Eq. (3) represents the dispersive properties of the sample. Commonly, the dependence of the refractive index of a material with wavelength is expressed by the Sellmeier

#251546 Received 8 Oct 2015; revised 1 Dec 2015; accepted 1 Dec 2015; published 18 Dec 2015

equation [11]. Here, we make a polynomial expansion of n around k_c, the center wavenumber of the source spectrum $S(k)$:

$$n(k) = \sum_{j=0}^{J} n_j \left(\frac{k-k_c}{k_c} \right)^j, \tag{4}$$

with a total number of coefficients $J \in \mathbb{N}$. Based on the literature values for the parameters of the Sellmeier equation or experimental data presenting $n(\lambda)$, the coefficients n_j of the polynomial expansion can be determined using a fit. Another common way to describe the dispersive properties of a material is in terms of the group refractive index and the GVD. At the center wavenumber, these are given by $n_g(k_c) = n(k) + k(\mathrm{d}n/\mathrm{d}k)|_{k=k_c}$ and $GVD(k_c) = 1/c^2(\mathrm{d}n_g/\mathrm{d}k)|_{k=k_c}$, respectively. Here c is the speed of light.

The dependence of $n(k)$ on k, from Eq. (4), causes the oscillations of the cosine in Eq. (3) to be non-linear. For the attenuation analysis (Section 2.3) and for the dispersion estimation, the phase of the signal of Eq. (3) has to be extracted. Therefore the analytical signal of the interference signal is calculated [12, 13], which is given by

$$\widetilde{I_{int}}(k) = I_{int}(k) + i\mathscr{H}\{I_{int}(k)\}, \tag{5}$$

where $\mathscr{H}\{\cdot\}$ denotes the Hilbert transform operator. The phase of $\widetilde{I_{int}}(k)$ can then be determined by

$$\varphi(k) = \tan^{-1}\left(\frac{\mathscr{H}\{I_{int}(k)\}}{I_{int}(k)} \right), \tag{6}$$

which is equal to the argument of the cosine expression in Eq. (3) performing a Taylor expansion of $\varphi(k)$ around k_c and combining this with the polynomial expansion of $n(k)$ around k_c in Eq. (4) for $J = 2$, we obtain

$$\frac{\varphi(k)}{k_c L} = (n_0 - 1) + (n_0 - 1 + n_1)\left(\frac{k-k_c}{k_c} \right) + (n_1 + n_2)\left(\frac{k-k_c}{k_c} \right)^2. \tag{7}$$

The coefficients of Eq. 7 can be determined by fitting $\varphi(k)$ with a polynomial. From the fit parameters coefficients, n_0 and n_1, are determined and the group refractive index follows as $n_g(k_c) = n_0 + n_1$ and the group velocity dispersion $GVD(k_c) = 2(n_1 + n_2)/(k_c c^2)$.

In the z-domain, the dispersion leads to a broadening of the transmission peaks. Using the complex notation of the analytical signal it is easy to see that the phase can be linearized by multiplying the Hilbert transformed interference signal with $\exp[i\Delta\varphi(k)]$, where $\Delta\varphi(k) = \varphi(k) - \varphi_{\mathrm{linear}}(k)$ [13]. The dispersion corrected signal in the z-domain is given by the inverse Fourier transform of the dispersion corrected analytic signal

$$I_c(z) = \mathscr{F}^{-1}\{|\widetilde{I_{int}}(k)| \exp[i\Delta\varphi(k)]\}, \tag{8}$$

where $\mathscr{F}^{-1}\{\cdot\}$ denotes the inverse Fourier transform of the given signal.

2.3. Attenuation coefficient

After dispersion correction, the attenuation coefficient can be determined both from the spectral or spatial domain signal. Taking the inverse Fourier transform of Eq. (3) and assuming the attenuation does not vary a lot over the spectral bandwidth of the system, i.e. $\mu_t(k) = \mu_t$, we obtain an equation for the spatial domain transmission OCT signal

$$a(z) = \alpha(1-\alpha)\exp\left(-\frac{1}{2}L\mu_t\right)\mathscr{F}^{-1}\{E_s^2(k)\}(z) \otimes [\delta(z - L(n_g - 1)) + \delta(z + L(n_g - 1))], \tag{9}$$

#251546 Received 8 Oct 2015; revised 1 Dec 2015; accepted 1 Dec 2015; published 18 Dec 2015

where $\otimes$ denotes a convolution. Performing a reference measurement with attenuation $\mu_t = 0$ and a measurement on the sample, one obtains two z-domain signals. The signal of the sample differs from that of the reference measurement by a possible shift of the delta functions and a change in height, caused by the optical attenuation. From Eq. (9) it can be deduced that the attenuation coefficient can be determined by measuring the height of the peak in the z-domain of the reference and sample measurements, a_{ref} and a_{sam}, respectively, and using

$$\mu_t = \frac{2}{L} \ln \left(\frac{\max|a_{ref}|}{\max|a_{sam}|} \right). \tag{10}$$

The attenuation coefficient thus obtained is an average over the spectral bandwidth of the system. The spatial domain analysis offers the advantage of path-length selectivity. In this way the ballistic light can be filtered from the scattered light, which can then be used to estimate the attenuation μ_t and the refractive index of the sample.

Alternatively, from Eq. (3) and Eq. (8) the absolute value of the analytical signal can be recognized as the complex magnitude of the interference signal

$$|\widetilde{I_{int}}(k)| = \alpha(1-\alpha)E_s^2(k) \exp\left(-\frac{1}{2}L\mu_t(k)\right). \tag{11}$$

The wavenumber dependent attenuation coefficient $\mu_t(k)$ can be determined by performing a reference and a sample measurement of $|\widetilde{I_{int}}(k)|$. Similar to Eq. (10), the ratio of these two signals then results in $\mu_t(k)$.

3. Methods

3.1. Experimental setup

The Fourier domain transmission OCT setup is depicted in Fig. 2. It is based on a Mach-Zehnder interferometer with spectral domain detection of the interference signal. A fiber based super-luminescent diode (D-1300-HP, Superlum) with a center wavelength of 1300 nm and a full width half maximum (FWHM) bandwidth of 110 nm is used as a light source. After collimation by an achromatic doublet lens (AC254-045-C-ML, Thorlabs), the light is split into the reference and sample arm by a 50/50 beamsplitter (BS015, Thorlabs). Optical power in the two arms is regulated by neutral density filters (NDC-100C-4M, Thorlabs) in each arm. The reference arm contains an optical delay line, that is tunable in length by means of a translation stage (PT1/M, Thorlabs). The sample arm contains two confocal 200 mm achromatic lenses (AC254-200-C-ML, Thorlabs). Samples are mounted in the focal point between the two lenses. After recombination by a second 50/50 beamsplitter the resulting beam is expanded by a 4-f lens system (AC254-060-C-ML and AC508-080-C-ML, Thorlabs) before being introduced to a spectrometer. A pinhole is placed at the focus position between the two lenses of the 4-f system to remove any stray light. Spectral domain detection is performed by a home build spectrometer, consisting of a holographic grating (1145 l/mm, Wasatch Photonics), an SWIR imaging lens (S5LPJ0037/360, Sill Optics), and a 76 kHz InGaAs linescan camera (GL2058L, Sensors Unlimited). Camera data is acquired using a framegrabber (PCIe-1433, National Instruments) and Labview software (National Instruments).

3.2. Setup calibration and performance

The spectrometer is calibrated using an Argon gas discharge lamp (AvaLight-CAL-AR, Avantes). The calibration lamp is placed on the free-side of the first beamsplitter of the interferometer. The emission spectrum of the lamp is recorded by the spectrometer and the measured emission lines are compared to reference values from literature. A third degree polynomial is

#251546 Received 8 Oct 2015; revised 1 Dec 2015; accepted 1 Dec 2015; published 18 Dec 2015

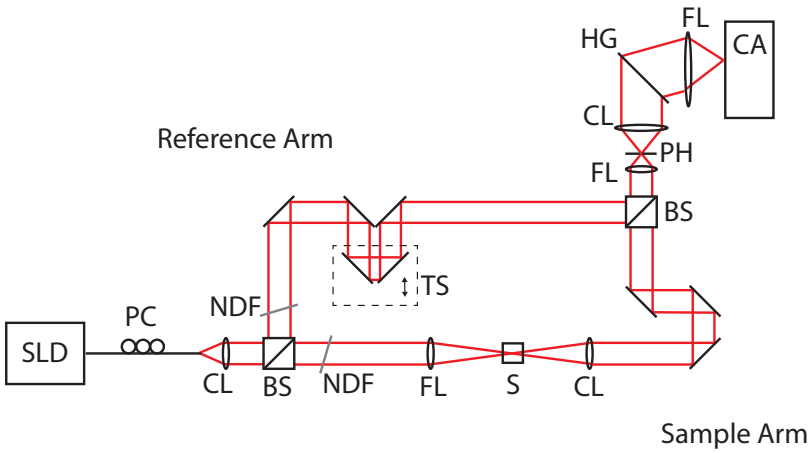

Fig. 2. Schematic diagram of the experimental setup. BS: beam splitter, CA: camera, CL: collimation lens, FL: focusing lens, HG: holographic grating, NDF: Neutral density filter, PC: polarization controller, PH: pinhole, S: Sample, SLD: superluminescent diode, TS: translation stage

fitted through the data to obtain a relation between pixel number and wavelength. The performance of the transmission OCT system is checked using the movable delay line in the reference arm. This yields a maximum path length difference of 11.6 ± 0.1 mm. The axial resolution of the system is determined by measuring the FWHM of the signal peak in the z-domain with no sample in the interferometer. The measured axial resolution of the system is 18 ± 1 μm, (bandwidth limited). The lateral point spread function, measured in air, has an in-focus FWHM waist of 32.8 ± 0.7 μm. Following the definition of Nassif et al. [14], the roll-off parameter of the system is $w = 2.1 \pm 0.1$. Measurements using neutral density filters show a signal sensitivity of -106 dB.

3.3. Sample preparation and measurement

Measurements of n_g and the GVD are performed on both liquid samples and glass plates. The glass plates provide a good validation as the optical material properties for glasses are well known. Four different glass plates are used in the experiments; N-BK7 (WG11050, Thorlabs), sapphire (WG31050, Thorlabs), UV-fused silica (WG41050, Thorlabs) and calcium fluorite (WG51050, Thorlabs). All glass plates are 5 mm thick and uncoated. Liquid samples used for the refractive index measurements are: ethanol (32221, Sigma-Aldrich), de-mineralised water and glucose solutions. These liquids were measured using a 10 mm path length, fused quartz cuvette (CV10Q3500F, Thorlabs) placed in the sample arm. Refractive index data is obtained after averaging of 5000 measurements per sample.

Measurements of attenuation are performed on monodisperse silica particle suspensions and on de-mineralised water. Two different particle sizes are considered; 0.5 μm and 1.5 μm diameter. Silica particles (KI-PSI-0.5P and KI-PSI-1.5P, Kisker Biothech) in powdered form are suspended in de-mineralised water containing 0.3 mM of sodium dodecyl sulphate to prevent aggregation [10]. Suspensions are vortexed for 60 minutes and sonicated for 30 minutes before measurements. All silica particle suspensions are measured in a 1 mm path length cuvette (Z802689-1EA, Sigma-Aldrich) mounted in the sample arm. Calculating the attenuation coefficient for the silica particle suspensions, water is used as a reference in Eq. (10). In this way the difference in attenuation between the suspension and water is obtained, removing the contribu-

#251546 Received 8 Oct 2015; revised 1 Dec 2015; accepted 1 Dec 2015; published 18 Dec 2015

tion of the water absorption to the total attenuation of the sample. Leaving only the scattering contribution by the silica particles $\mu_t = \mu_s$. For all the measurements of silica particle suspensions, including the water reference, 100000 measurements are averaged. The wavelength dependent absorption coefficient of water is determined from 1000 spectra.

The particle-sizes are measured using a Malvern Zetasizer, obtaining a mean diameter of 1138 ± 48 nm for the KI-PSI-1.5P particles and 426.6 ± 61.5 nm for the KI-PSI-0.5P particles. These measured sizes are smaller than the factory values, but are consistent with electron microscopy measurements on the same products from the same manufacturer [10].

3.4. Data analysis algorithm

After acquisition the spectral data is stored in raw binary format. It is analyzed using software written in MATLAB (Mathworks, R2014b). An overview of the data processing flow is presented in Fig. 3. The data acquisition includes a measured spectrum $I(k)$, a spectrum of the reference arm only, $I_{ref}(k)$, and a spectrum for the sample arm only, $I_{sam}(k)$. Furthermore the calibrated wavenumber k is obtained from a combination of the spectrometer calibration and an optimization algorithm. The polynomial coefficients of the wavenumber calibration is optimized with respect to the group index of water using a trust-region algorithm (MATLAB function *fminunc*). The third order polynomial coefficients of the spectrometer calibration are used as the initial parameter estimate.

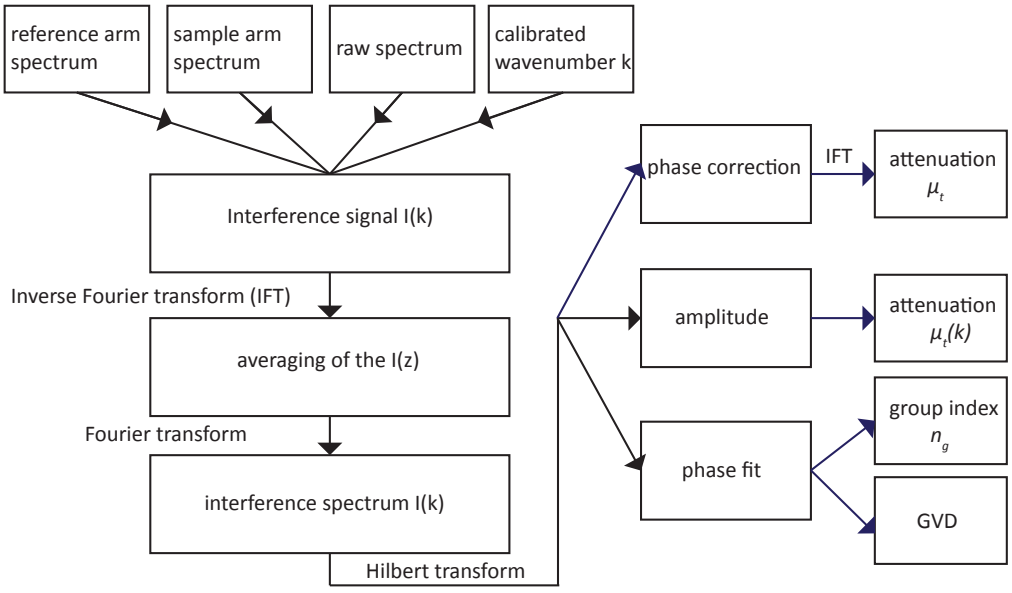

Fig. 3. Schematic illustration of the analysis algorithm for the determination of the optical material properties.

As spectrum containing only the interference contribution is generated by subtracting all other contributions, $I_{int}(k) = I(k) - I_{ref}(k) - I_{sam}(k)$. To obtain the average interference spectrum this signal is inverse Fourier transformed, averaged and transformed back. For determination of the analytic signal, Eq. (5), the built-in MATLAB function *hilbert* is used. Furthermore, the function *phase* is used to determine and unwrap the phase of the given signal. The phase of the signal is cropped in k by choosing the relative heights of the envelope signal with respect to the peak of the envelope to be larger than 0.25. The phase analysis uses the built-in MATLAB

#251546 Received 8 Oct 2015; revised 1 Dec 2015; accepted 1 Dec 2015; published 18 Dec 2015

function *fit* to fit a cubic polynomial, Eq. (7) using the generalized least squares to the difference of the measured phase and a reference phase versus k.

3.5. Dependent scattering calculations

Calculations of the scattering coefficient are performed using a Mie theory [15] and a dependent scattering model. The effect of dependent scattering is taken into account using the structure factor for computation of the scattering efficiency ratio following the work of Nguyen et al. [10]. Although dependent scattering does not take the effects of multiple scattering into account, the model is appropriate for describing the reduction of power of the ballistic light. Only the ballistic photons that scatter for the first time reduce this power. Interactions between multiply scattered light will only affect our path-length distribution at path-lengths beyond that of the ballistic light.

The dependent scattering model uses the Percus-Yevick model to compute the radial distribution function, which accounts for interactions between particles. Furthermore, we assume the Rayleigh-Debye condition is valid, i.e. the scattering particles can be treated as point scatterers. Input to the dependent scattering calculation are the refractive indices of the medium and the suspended particles, the wavelength of the light, the experimentally determined particle radius and the concentration of the particles.

4. Results

A typical set of averaged transmission OCT measurements through a fused silica glass slide is shown in Fig. 4. Figure 4(a) shows the raw interferometric signal versus wavenumber. The instantaneous phase obtained through Hilbert transform of the interference spectrum is shown in Fig. 4(b). A linear relation between the start and end point is added to show the non-linearity of the phase. The non-linear behavior of the phase is caused by the cumulative effects of the material dispersion and by the spectrometer dispersion, both indicated. The phase difference between the linear phase and the phase signal from Fig. 4(b) is depicted in Fig. 4(c).

The parabolic shape is clearly visible and caused by the large values of $n_1 + n_2$ for fused silica glass and by the non-linearity of the spectrometer. The phase after spectrometer correction (red) has a lower maximum compared to the raw phase signal and shows a more pure parabolic phase behavior. The measured and compensated signal after the Fourier transformation is shown in 4(d), where the peak position represents the path length of the ballistic light. Due to dispersion, the measured transmission OCT signal (blue, dashed) is decreased and broadened compared to the dispersion compensated signal (red).

4.1. Refractive index and group velocity dispersion quantification for glasses and liquids

Figure 5 shows the dispersion results of four different glasses: BK7, fused silica, sapphire and calcium fluoride (CaF_2), and two liquids: water and ethanol. Figure 5(a) shows the results for the group refractive index for the different materials. The red bars denote the measured values using transmission OCT. It can be seen that the group refractive indices are close to the values from literature [11, 16–28]. BK7, fused silica and CaF_2 are slightly underestimated compared to the literature values, whereas for sapphire a relatively large underestimation of 3.2 percent is observed. Water has a slight overestimation of 0.56 percent and for ethanol the underestimation is 2.5 percent. The group velocity dispersion is shown in Fig. 5(b). It can be seen that the group velocity dispersion of all materials, except fused silica, are somewhat overestimated compared to the literature values. For fused silica the group velocity dispersion values are spread between the literature values.

Aqueous solutions with different concentrations of glucose are measured to determine the optical properties of the constituent materials (as shown in Fig. 6). Both the group refractive

#251546 Received 8 Oct 2015; revised 1 Dec 2015; accepted 1 Dec 2015; published 18 Dec 2015

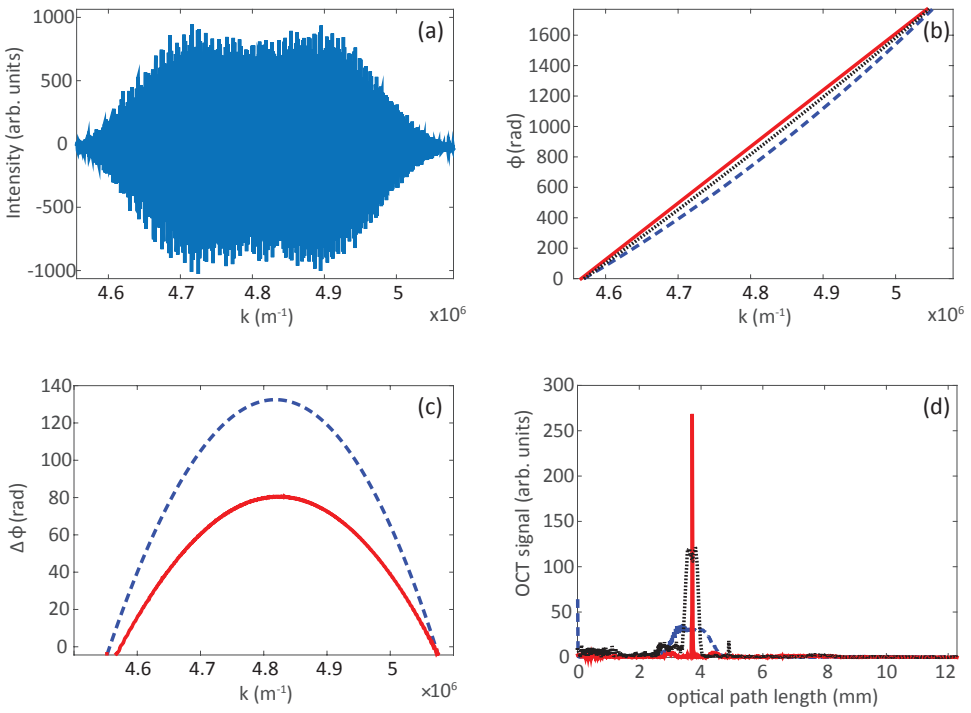

Fig. 4. Overview of the data processing steps for the fused silica sample (a) Reference and sample arm subtracted interference spectrum. (b) Phase of the original Hilbert transformed signal (blue, dashed), the spectrometer corrected signal (black, points), and the linear phase relation (red). (c) Phase difference between the linear phase and the original signal (blue, dashed) and to the setup dispersion corrected signal (red, solid). (d) z-Domain transmission OCT signal after inverse Fourier transform without dispersion correction (blue, dashed), after setup dispersion correction (black, points) and after material dispersion correction (red, solid).

index and the GVD follow a linear relation as would be expected from a volume-weighted average of the optical properties. The slope of $(1.21 \pm 0.02)10^{-3}$ group index change per volume percent results in a group refractive index of pure glucose of 1.465 ± 0.004, which agrees well with literature values [29,30]. The slope of $(-2.05 \pm -0.04)\,10^{-28}\,\mathrm{s}^2/\mathrm{m}$ GVD change per volume percent results in a GVD of pure glucose of $(-7.34 \pm 0.04)\,10^{-26}\,\mathrm{s}^2/\mathrm{m}$.

4.2. Attenuation and scattering measurements of silica particle suspensions

Transmission OCT measurements are performed for suspensions of silica particles in different concentrations. Two different particles sizes are considered; 0.5 µm and 1.5 µm diameter. Typical spatial domain data, averaged over 100000 measurements, for the 0.5 µm and 1.5 µm particles are shown in Fig. 7(a) and Fig. 7(b), respectively. For every concentration, peaks can be observed corresponding to ballistic light transmission. As the concentration of scatterers increases the peak amplitude decreases and the peak moves slightly to longer path lengths. In addition a decaying tail is observed behind the ballistic transmission peak of the 1.5 µm particle suspensions. This tail gradually becomes predominant as the concentration of scatterers increases and is caused by forward scattered light transmitted through the sample. The 0.5 µm

#251546 Received 8 Oct 2015; revised 1 Dec 2015; accepted 1 Dec 2015; published 18 Dec 2015

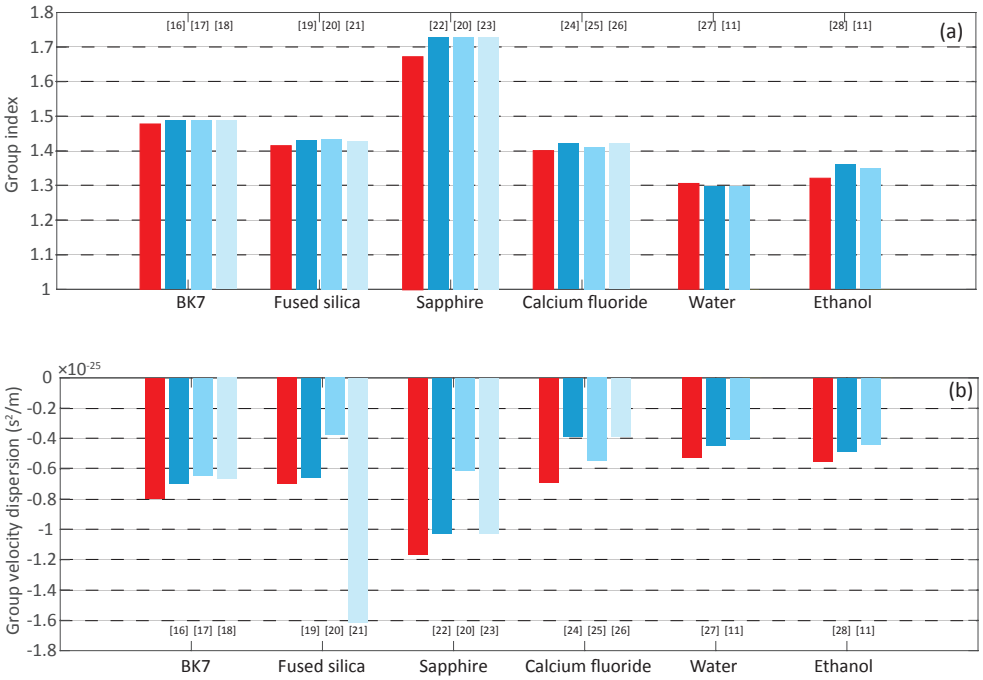

Fig. 5. Measured group refractive index (a) and group velocity dispersion (b) compared with literature values. The measured values are denoted in red and the literature values are visualized in shades of blue with the reference indicated above and below their respective bar.

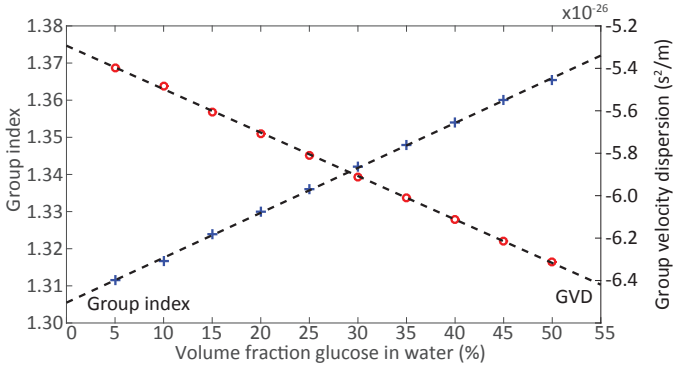

Fig. 6. Group index and group velocity dispersion for solutions with varying glucose concentration as determined with transmission OCT. The measurements (indicated with open symbols, red and blue) are fitted with a linear regression (dashed black lines).

#251546 Received 8 Oct 2015; revised 1 Dec 2015; accepted 1 Dec 2015; published 18 Dec 2015

particles have a much lower scattering coefficient and scattering anisotropy and do not show the scattered light in the transmission OCT signal.

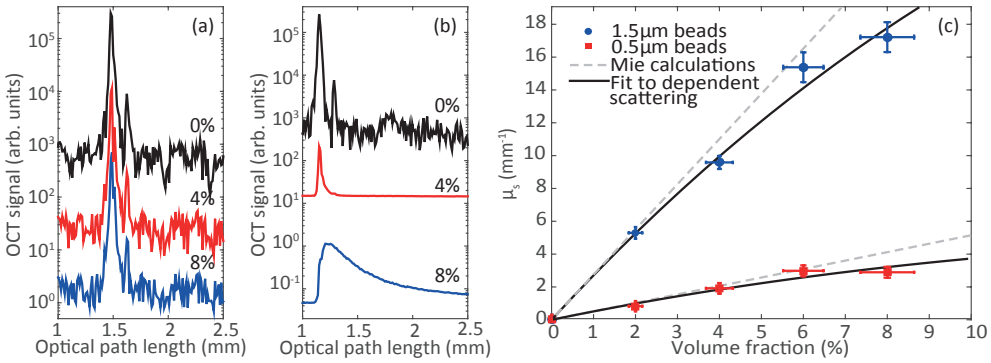

Fig. 7. Spatial domain transmission OCT data for several concentrations of 0.5 µm (a) and 1.5 µm (b) silica particles in water. Data separated for plotting by multiplication with powers of 10. (c) Measured scattering coefficients for the silica suspensions. The data is fitted using a dependent scattering model (black, solid), which is based on Mie calculations (gray, dashed).

The measured scattering coefficient μ_s as function of the concentration for the 0.5 µm and 1.5 µm silica particle suspensions are shown in Fig. 7(c). For higher concentrations of particles in the suspension, more light is scattered resulting in an increase of the scattering coefficient. At very high concentrations the linear relation between scattering coefficient and particle concentration does not hold and the data is best described by a dependent scattering model. A fit of this model (Section 3.5) with the refractive index of the particles as the free parameter, results in $n_0 = 1.430 \pm 0.009$ for the 0.5 µm particles, and $n_0 = 1.444 \pm 0.005$ for the 1.5 µm particles. This value is close to the value of the phase refractive index of 1.447 for fused silica, reported by Malitson [19].

The Hilbert transform method is used to determine the wavelength dependent attenuation coefficient for de-mineralised water and the 2 vol.% suspension of 1.5 µm particles. The measured absorption spectrum of water is shown in Fig. 8(a). The measured absorption coefficient agrees well with the data from Kedenburg et al. The wavelength dependent scattering coefficient for the silica particle suspension is shown in Fig. 8(b). Dependent scattering calculations are performed over the spectral range for comparison to the measured data. The measured data agree well with the calculated data. In both the water and the particle suspension data, deviations are observed at the edges of the measured attenuation spectra. At these wavelengths the source intensity is low resulting in small signals.

5. Discussion

We showed transmission OCT measurements of n_g, the GVD and the (wavelength resolved) attenuation coefficient. The measurements on glass plates, liquids and glass particle suspensions validated the proposed analysis technique.

The measurements of n_g showed good agreement with values found in literature. Some variation was present in the literature data, possibly caused by differences in the materials used. Our results are slightly less accurate compared to the refractive index measurement of Dirckx et al. [7] and Zvyagin et al. [6]. The GVD measurements, in general, agree well with literature values. Due to the large spread in values reported in literature, exact estimation of the accuracy of our method is difficult. For most measurements the obtained value for the GVD is within the

#251546 Received 8 Oct 2015; revised 1 Dec 2015; accepted 1 Dec 2015; published 18 Dec 2015

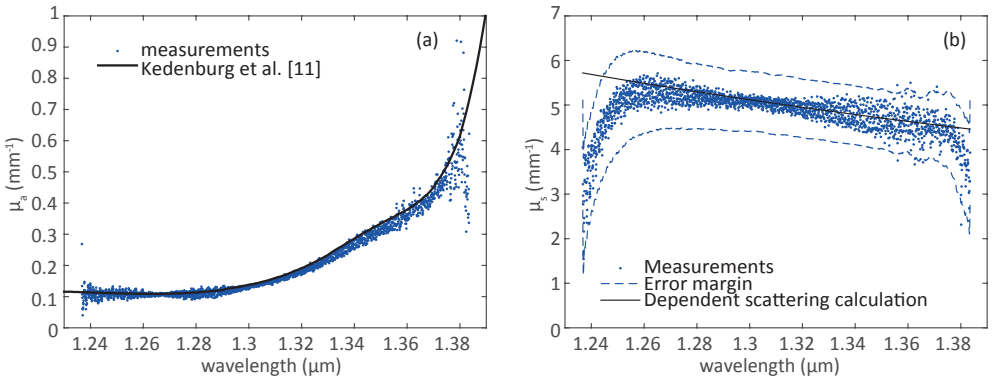

Fig. 8. (a) Measured absorption coefficient of water versus wavelength (blue, dots) and its comparison to literature [11] (black, solid). (b) Measured scattering coefficient versus wavelength for 2 vol.% 1.5 μm silica particles (blue, dots). Error margin is denoted by the dashed lines. The data is compared to the scattering coefficient obtained from dependent scattering calculations (black, solid).

variation represented in literature. We observed that the measured values of n_g and the GVD are very sensitive to variations in the spectrometer calibration. More accurate measurements can be obtained by improving the spectrometer calibration procedure. Increasing the bandwidth of the setup and the thickness of the samples could also provide more accurate results for n_g and GVD. We observed that the exact choice of the cropping factor affects our estimates of both n_g and GVD. The choice of 0.25 resulted in the most accurate estimation of both group velocity index and GVD. Measurement of n_g and the GVD for glucose solutions showed a clear linear behavior over the measured concentration range. By avoiding positioning errors and realignment of the cuvette, possible alignment errors are circumvented. Hence, the glucose measurements show that small differences in refractive index can be measured. The lowest glucose concentration measurable is 0.39 vol. % and was estimated by a linear extrapolation of the slope and comparison to the error in the measurements. This concentration is still larger than typical blood glucose concentrations.

Determination of the attenuation coefficient is shown for both z-domain and spectral domain analysis. For both methods the main experimental difficulty proved to be the prevention of particle aggregation in the suspensions. The z-domain method works in principle up to 20 mean free paths (MFP) of attenuation. The technique is limited to scattering anisotropies up to approximately 0.9. Large anisotropy factors, as for example is the case for tissue, make the discrimination between ballistic and single scattered photons difficult. Increasing the spectral bandwidth results in a more narrow axial point spread function, which facilitates discrimination of ballistic light from scattered light. Additionally, information can be retrieved from the scattered light distribution, either by using a total attenuation coefficient or fitting a scattering model.

Wavelength resolved attenuation coefficients are computed from spectral domain data for water and 2 vol.% of the 1.5 μm particle suspension. The results show good agreement with literature and simulated data respectively. Deviations between measurements and literature are observed at the edges of the spectra. We attribute this to the low power of the light source at these wavelengths which makes it difficult to retrieve the envelope of the measured spectrum using the Hilbert transform. For a similar reason, measurements on samples with high attenuation coefficients (larger then approximately 10 MFP) fail to give accurate results. For highly attenuating samples short time Fourier transform techniques can be applied in combination with

#251546 Received 8 Oct 2015; revised 1 Dec 2015; accepted 1 Dec 2015; published 18 Dec 2015

an analysis in the z-domain. This provides the benefit of path length discrimination, however, at the cost of reduced spectral resolution.

The measurements presented in this article demonstrate the potential of Fourier-domain transmission OCT as a powerful and versatile platform for measurements of optical properties. Transmission OCT does not rely on scattered light to perform a measurement, and therefore is not based on complicated light transport models or requires a homogeneous sample. In addition, coherence gating provides a means to filter or select scattered from the ballistic light from the measured signal.

Application of the presented techniques can provide a way to optically characterise tissue in biopsies, aiding in the diagnostics of diseases. The multiple modes of contrast provided by our technique can provide a great advantage in this respect. In addition, transmission OCT can provide compact and cost effective measurements in microfluidics and lab-on-a-chip applications. With the onset of OCT on a chip technology this technique can provide a compact, versatile and relatively cheap way to measure optical properties. In addition, the proposed methods for determining n_g and the GVD also can be applied in backscattering OCT, possibly providing additional (functional) tissue contrast. The measurements presented in this paper concern the characterization of the optical properties of a homogeneous bulk sample. The use of transmission OCT can be extended towards imaging spatially varying optical properties using computed tomography techniques.

6. Conclusion

In conclusion, we presented Fourier-domain transmission OCT as a method for measuring the group refractive index, the group velocity dispersion and the wavelength resolved attenuation coefficient of a wide range of samples. We validated the proposed methods using experimental data. The measurements are in good agreement with literature values and analytical theory. We showed that transmission OCT provides a powerful tool for measurements of various optical properties.

Acknowledgments

This research is supported by the Dutch Technology Foundation STW, which is part of the Netherlands Organisation for Scientific Research (NWO), and which is partly funded by the Ministry of Economic Affairs. We thank Prof. L. J. van Vliet for useful discussions.

#251546 Received 8 Oct 2015; revised 1 Dec 2015; accepted 1 Dec 2015; published 18 Dec 2015